REPORT DOCUMENTATION PAGE	Form Approved OMB NO. 0704-0188

1. REPORT DATE (DD-MM-YYYY)
27-12-2019

2. REPORT TYPE
Final Report

3. DATES COVERED (From - To)
1-May-2017 - 29-Dec-2019

4. TITLE AND SUBTITLE
Final Report: Improved Ceramic Manufacturability With Electric Field Assisted Sintering: Developing Underlying Principles

5a. CONTRACT NUMBER
W911NF-17-1-0223

5b. GRANT NUMBER

5c. PROGRAM ELEMENT NUMBER
611102

6. AUTHORS

5d. PROJECT NUMBER

5e. TASK NUMBER

5f. WORK UNIT NUMBER

7. PERFORMING ORGANIZATION NAMES AND ADDRESSES
Massachusetts Institute of Technology (MIT
77 Massachusetts Avenue
NE18-901
Cambridge, MA 02139 -4307

8. PERFORMING ORGANIZATION REPORT NUMBER

9. SPONSORING/MONITORING AGENCY NAME(S) AND ADDRESS (ES)
U.S. Army Research Office
P.O. Box 12211
Research Triangle Park, NC 27709-2211

10. SPONSOR/MONITOR'S ACRONYM(S)
ARO

11. SPONSOR/MONITOR'S REPORT NUMBER(S)
70957-MS.1

12. DISTRIBUTION AVAILIBILITY STATEMENT
Approved for public release; distribution is unlimited.

13. SUPPLEMENTARY NOTES
The views, opinions and/or findings contained in this report are those of the author(s) and should not contrued as an official Department of the Army position, policy or decision, unless so designated by other documentation.

14. ABSTRACT

15. SUBJECT TERMS

16. SECURITY CLASSIFICATION OF:
a. REPORT UU
b. ABSTRACT UU
c. THIS PAGE UU

17. LIMITATION OF ABSTRACT
UU

15. NUMBER OF PAGES

19a. NAME OF RESPONSIBLE PERSON
Harry Tuller

19b. TELEPHONE NUMBER
617-253-6890

Standard Form 298 (Rev 8/98)
Prescribed by ANSI Std. Z39.18

RPPR Final Report
as of 02-Jan-2020

Agency Code:

Proposal Number: 70957MS **Agreement Number: W911NF-17-1-0223**

INVESTIGATOR(S):

Name: Harry Tuller
Email: tuller@mit.edu
Phone Number: 6172536890
Principal: Y

Organization: **Massachusetts Institute of Technology (MIT)**
Address: 77 Massachusetts Avenue, Cambridge, MA 021394307
Country: USA

DUNS Number: 001425594 EIN: 042103594
Report Date: 29-Mar-2020 Date Received: 27-Dec-2019
Final Report for Period Beginning 01-May-2017 and Ending 29-Dec-2019
Title: Improved Ceramic Manufacturability With Electric Field Assisted Sintering: Developing Underlying Principles
Begin Performance Period: 01-May-2017 **End Performance Period:** 29-Dec-2019
Report Term: 0-Other
Submitted By: Harry Tuller Email: tuller@mit.edu
Phone: (617) 253-6890
Distribution Statement: 1-Approved for public release; distribution is unlimited.

STEM Degrees: 1 **STEM Participants:** 2

Major Goals: High density ceramics maximize strength, translucency, thermal conductivity and provide gas tight environments. These features are key to applications ranging from armor, IR missile domes, integrated circuit substrates and solid oxide fuel cell electrolytes, respectively. To achieve desired high densities for such highly refractory materials, sintering (at times requiring hot isostatic pressing) must be performed at temperatures often in excess of 1500 °C for extended periods of time, leading to high costs, need for specialized facilities and incompatibility with less refractory materials. While conventional densification methods utilizing high temperature and pressure have reached their limits, electric field assisted sintering has demonstrated great potential in reducing temperature constraints imposed on ceramic materials during sintering. Application of electrical fields during sintering can reduce densification temperatures from above 1300 °C to 800 °C, to times as short as seconds, the latter via Flash Sintering (FS). While there have been many phenomenological observations and demonstrations of Field Assisted Sintering (FAST), reliable micro and nanoscale descriptions remain lacking (1). This is not surprising given that the electrical and mass transport properties of ceramic materials differ so widely, ranging from highly insulating to metallic, from predominantly ionic to electronic conductors and all with properties highly dependent on microstructure. Here we address this challenge by investigating model titania-based ceramics in which we 1) systematically vary the ionic and electronic defects and thereby the underlying factors controlling both densification and electrical properties, 2) monitor the development of conductive pathways and thereby microstructure by in-situ frequency dependent complex impedance spectra during densification both with and without applied fields and 3) support the analysis of experiments by performing atomistic modeling to understand and predict how defect formation and transport are modified under applied external fields and in the vicinity of space charge fields accompanying grain boundaries. Progress along these lines provide considerable insights into the factors contributing to and controlling FAST processes.

The overall objective is to reveal the dominant mechanisms governing field assisted sintering as a function of material electrical properties, microstructure evolution and environmental conditions. The approach involves examination of a model system based on TiO_2 in which cation diffusion and electronic conductivity can be systematically controlled by dopants and oxygen partial pressure, supported by in-situ electrical characterization during sintering via complex impedance spectroscopy. The experimental results are further supported by first-principles calculations of electric field modified defect concentrations and mobilities, thereby allowing for more detailed analysis of results and projections for other conditions and materials.

Accomplishments: This project allowed us to gain greater insights into the underlying mechanisms that occur during field assisted sintering. Using TiO_2 as a model system allows one to engineer the main defect types and concentrations through doping and pO_2 management. The modeling of the migration barrier for diffusion of Ti defects shows that interstitials diffuse considerably faster than Ti vacancies, and that an external electric field, such

as those used in flash sintering experiments (500 V·cm-1), has little influence on the migration barrier. Consequently, the leading mechanism explaining enhanced sintering under electrical bias can be attributed largely to Joule heating. The effect of the space charge at the grain boundaries was also modeled in the case of donor or acceptor doped TiO_2, and showed that grain boundaries are electronically blocking in Ta-doped TiO_2 and conducting in Ga-doped TiO_2, which can also play an important role related to heat dispersion induced by Joule heating. We also show that an applied electric field will be non-homogeneous in Ga-doped TiO_2 because of carrier redistribution. The flash sintering experiments were found to be difficult to reproduce due to the generation of non-homogeneous current pathways via conductive filaments. The temperatures reached during flash are potentially high enough to trigger local melting of TiO_2. Measurements of field assisted sintering with moderate applied electric fields makes the study of the influence of defect concentration on sintering feasible. With the two strategies considered, i.e. pellets and thick film measurements, we show that sintering is enhanced when Ti interstitials are the dominant defects, in accordance with the results of defect migration barrier modeling
Summarizing the key findings of this study, field assisted sintering of semiconducting oxides is largely driven by joule heating. Optimum results can be expected, i.e. lowest furnace temperature and shortest sintering times, when dopants and oxygen partial pressure are selected that support the fastest migrating ionic species limiting densification. Furthermore, selection of geometry is critical in insuring that sufficient Joule heating is achieved and that current flow is uniform across the densifying ceramic element.

Training Opportunities: There were 4 supporting personnel on the program. Dr. Clement Nicollet - post doctoral research associate, Jing Yang and Minh Dinh, PhD candidates and a masters level visiting scientist Tamar Kadosh who is applying for admission to MIT as a doctoral student. Dr. Nicollet had the opportunity to extend his processing and electrochemical studies on fuel cell materials towards these sintering studies. In the process, he had the opportunity to extend his familiarity with defect chemical and transport studies, different ways to examine sintering and densification and operating dilatometers while simultaneously applying fields and measuring electrical properties in-situ. He also gained the opportunity to work in collaboration with theorists and to manage aspects of the program including the supervision of Tamar Kadosh. Jing Yang and Minh Dinh, both students of Prof. Yildiz had the opportunity to apply first principles modeling to a materials system with a well defined objective of understanding a) the role of defects and their diffusive properties in relation to sintering and b) the impact of fields on both defect formation and diffusion. Tamar Kadosh played a supportive role in preparing specimens but also in running the densification studies on the screen printed materials. As such she gained a much clearer appreciation of how to approach more focused and sophisticated research.

Results Dissemination: An invited talk was given by Prof. Yildiz at the Fall 2018 Material Research Society meeting in Boston during December of 2018

Several publications are now under preparation

Honors and Awards: Professor Harry Tuller was awarded the 2019 Thomas Egleston Medal of Columbia Engineering. "The Medal is in recognition of distinguished achievement of a Columbia Engineering alum in engineering or applied science. The recipient must have significantly advanced his or her field of the engineering profession or the management of engineering activities"

Prof Harry Tuller was awarded MIT's Committed to Caring award that recognizes that in graduate school, advisors and mentors set the tone for student experiences, and positive faculty support has the ability to shape student research and lives for the better. This award honors professors who build inclusive cultures in their labs and classrooms, who support their students' mental and emotional health, and who actively support their students' scholarly pursuits.

Protocol Activity Status:

Technology Transfer: An MIT invention disclosure was filed on "Light-assisted flash sintering: fundamentals and applications of 3D-enabled printing of ceramic materials" with conception date of 5/20/19

PARTICIPANTS:

Participant Type: PD/PI
Participant: Harry Louis Tuller
Person Months Worked: 4.00 **Funding Support:**

Project Contribution:
International Collaboration:
International Travel:
National Academy Member: N
Other Collaborators:

Participant Type: Co PD/PI
Participant: Bilge Yildiz
Person Months Worked: 3.00 **Funding Support:**
Project Contribution:
International Collaboration:
International Travel:
National Academy Member: N
Other Collaborators:

Participant Type: Postdoctoral (scholar, fellow or other postdoctoral position)
Participant: Clement Nicollet
Person Months Worked: 7.00 **Funding Support:**
Project Contribution:
International Collaboration:
International Travel:
National Academy Member: N
Other Collaborators:

Participant Type: Graduate Student (research assistant)
Participant: Jing Yang
Person Months Worked: 6.00 **Funding Support:**
Project Contribution:
International Collaboration:
International Travel:
National Academy Member: N
Other Collaborators:

Participant Type: Graduate Student (research assistant)
Participant: Minh Dinh
Person Months Worked: 4.00 **Funding Support:**
Project Contribution:
International Collaboration:
International Travel:
National Academy Member: N
Other Collaborators:

Participant Type: Non-Student Research Assistant
Participant: Tamar Kadosh
Person Months Worked: 4.00 **Funding Support:**
Project Contribution:
International Collaboration:
International Travel:
National Academy Member: N
Other Collaborators:

RPPR Final Report
as of 02-Jan-2020

Improved ceramic manufacturability with electric field assisted sintering: Developing underlying principles

Award W911NF1710223

ARO/GOR: Dr. Michael Bakas

Dates: May 1, 2017 - June 30, 2019

Principle Investigator: Professor Harry L. Tuller (Department of Materials Science and Engineering, Massachusetts Institute of Technology
Co-Principle Investigator: Professor Bilge Yildiz (Departments of Nuclear Science and Engineering and Materials Science and Engineering, Massachusetts Institute of Technology

Research Team: Dr. Clement Nicollet, Tamar Kadosh, Jing Yang, Minh Dinh.

1 Introduction and objectives

High density ceramics maximize strength, translucency, thermal conductivity and provide gas tight environments. These features are key to applications ranging from armor, IR missile domes, integrated circuit substrates and solid oxide fuel cell electrolytes, respectively. To achieve desired high densities for such highly refractory materials, sintering (at times requiring hot isostatic pressing) must be performed at temperatures often in excess of 1500 °C for extended periods of time, leading to high costs, need for specialized facilities and incompatibility with less refractory materials. While conventional densification methods utilizing high temperature and pressure have reached their limits, electric field assisted sintering has demonstrated great potential in reducing temperature constraints imposed on ceramic materials during sintering. Application of electrical fields during sintering can reduce densification temperatures from above 1300 °C to 800 °C, to times as short as seconds, the latter via Flash Sintering (FS). While there have been many phenomenological observations and demonstrations of Field Assisted Sintering (FAST), reliable micro and nanoscale descriptions remain lacking (1). This is not surprising given that the electrical and mass transport properties of ceramic materials differ so widely, ranging from highly insulating to metallic, from predominantly ionic to electronic conductors and all with properties highly dependent on microstructure. Here we address this challenge by investigating model titania-based ceramics in which we 1) systematically vary the ionic and electronic defects and thereby the underlying factors controlling both densification and electrical properties, 2) monitor the development of conductive pathways and thereby microstructure by in-situ frequency dependent complex impedance spectra during densification both with and without applied fields and 3) support the analysis of experiments by performing atomistic modeling to understand and predict how defect formation and transport are modified under applied external fields and in the vicinity of space charge fields accompanying grain boundaries. Progress along these lines provide considerable insights into the factors contributing to and controlling FAST processes.

The overall objective is to reveal the dominant mechanisms governing field assisted sintering as a function of material electrical properties, microstructure evolution and environmental conditions. The approach involves examination of a model system based on TiO_2 in which cation diffusion and electronic conductivity can be systematically controlled by dopants and oxygen partial pressure, supported by in-situ electrical characterization during sintering via complex impedance spectroscopy. The experimental results are further supported by first-principles calculations of electric field modified defect concentrations and mobilities, thereby allowing for more detailed analysis of results and projections for other conditions and materials.

2 Methods

2.1 Modeling

2.1.1 Bulk defect equilibria and cation diffusivity

DFT calculations are performed on rutile TiO_2 with Vienna Ab initio Simulation Package (VASP) [1-4]. The generalized gradient approximation (GGA) with Perdew-Burke-Ernzerhof (PBE) functional is used [5,6] with Hubbard U correction [7] of 4.2 eV applied on the 3d states of Ti. To calculate the formation energies of defects, we used a supercell containing 24 unit formula of TiO_2. We used an energy cut-off of 700 eV and a 2×2×2 *k*-point grid. Ionic structures are relaxed until the forces on atoms are less than 0.01 eV/ Å.

Defect formation energies obtained from DFT are further fed into a thermodynamic model to predict equilibrium defect concentrations. The details of the model can be found in Ref. [8]. We further computed the migration barriers of Ti interstitials and Ti vacancies, and computed the total Ti self-diffusivity following a random-walk diffusion model.

2.1.2 Defect formation enthalpies and migration barriers in electric field

We quantified the formation energies and migration barriers of Ti defects under electric field by first-principle base methods. Under the effect of an applied external electric field, ϵ, the electric formation enthalpy, H_f^e, of a defect with charge q, X^q, is given by [9]:

$$H_f^e[X^q,\epsilon] = E_f[X^q] - \epsilon\Delta P \tag{1}$$

Where ΔP depicts the change in the system's polarization due to the introduction of the defect under the effect of electric field.

The formation energy of a defect X in charge state q, X^q, is defined as [10]:

$$E_f[X^q] = E_{tot}[X^q] - E_{tot}[bulk] - \sum_i n_i\mu_i + q(E_V + \mu_e) \tag{2}$$

in which $E_{tot}[X^q]$ is the total energy of the system containing the defect X^q and $E_{tot}[bulk]$ is the total energy of the system containing no defect of the same supercell. The third term is the chemical potential of elements involved in the defect. Electron chemical potential, μ_e, which is measured relative to the edge of the valence band, E_V, is used to describe the electron reservoir.

By writing out the formation energies and migration barriers under an electric field, we are able to quantify the effect of the electric field on cation diffusivities in TiO_2.

2.1.3 Modeling space charge layer profile

We performed continuum-level modeling to obtain the space charge layer profiles across a grain boundary in Ta-doped and Ga-doped TiO_2. The model assumes a space charge potential of 0.3 V for the Ta-doped case and -0.3 V for Ga-doped TiO_2. Poisson's equation is solved assuming the intrinsic defects can freely redistribute in the space charge layer, while the dopant can only segregate to the grain boundary core. We further modeled the profile change under applied bias assuming only electric carriers can freely redistribute under applied bias. This model gives a picture of local potential and electric field distributions at grain boundaries in doped TiO_2 under an applied external electric field.

2.2 Experimental

2.2.1 Powder preparation

Doped TiO_2 powders were synthesized by mixing TiO_2 commercial powder (rutile) with Ta ethoxide in ethanol. The suspension was stirred and heated at 80 °C until complete evaporation of the ethanol was achieved. The resulting powder was then annealed at 1050ºC for 6 h to allow the dopant to diffuse homogeneously throughout the rutile structure. The phase purity was monitored by x ray diffraction utilizing a Panalytical Xpert pro diffractometer with a Bragg-Brentano geometry, using a copper source.

2.2.2 Sample preparation

Pellets of the different TiO_2 powders were prepared by pressing at 1 T/cm_2 in a 6 mm diameter die, and pre-sintered at 1050 °C for 6 h. The average thickness of the pellets was roughly 3 mm, and the initial relative density ≈ 60 %. Pt electrodes were brush painted on the two flat sides of the pellet and heated at 1050 °C for 1 h. Screen-printing: ink prepared by combingin powder mix with 1% ethylcellulose and 30% terpineol.

2.2.3 Sintering measurements

The sintering experiments were carried out in a modified dilatometer that included two electrodes that simultaneously allows for impedance measurements and the application of voltage and current. A thermocouple close to the sample measures the temperature. The oxygen partial pressure is controlled by mixing H_2 and N_2 with the aid of MKS gas flow controllers. The pO_2 is measured with a homemade YSZ/Pt sensor directly placed inside the measurement setup, adjacent to the sample.

3 Results

3.1 Modeling

In this section, we summarize the results obtained by computational modeling in three parts. First, we compare bulk defect concentrations, cation diffusivity, and electronic conductivity in undoped, Ta-doped, and Ga-doped TiO_2. Second, we discuss how the defect concentrations and cation diffusivities change under strong electric field. Last, we show the defect redistribution profiles at grain boundaries for doped TiO_2, and explain their implications for the transport properties of polycrystalline titania ceramics.

3.1.1 Modeling of TiO_2 defects concentrations and diffusivities

We predicted the equilibrium defect concentrations in bulk Rutile TiO_2 utilizing a first-principles based framework as provided in [8]. The resultant concentrations, as a function of oxygen partial pressure P_{O_2} , are shown in Figure 1. For intrinsic TiO_2 (Figure 1(a)), we observe that at high P_{O_2}, the dominant compensating mechanism is hole compensated by V_{Ti}''''. As P_{O_2} decreases, the compensating mechanism changes to V_{Ti}'''' compensated by $Ti_i^{\cdot\cdot\cdot\cdot}$ (Frenkel equilibrium), and at even lower P_{O_2}, $Ti_i^{\cdot\cdot\cdot\cdot}$ compensated by electrons. The transition occurs at higher P_{O_2} as temperature is increased. In other words, the range in which $Ti_i^{\cdot\cdot\cdot\cdot}$ dominates over V_{Ti}'''' is extended at higher temperature.

To understand the effect of donor and acceptor dopants in TiO_2, in Figure 1(b) and (c), we show the equilibrium defect profiles with 1% Ta and Ga doping, respectively. The Ta donor predominantly substitutes in TiO_2 on Ti sites in the form of $Ta_{Ti}^{\cdot}$, which is compensated at these lower temperatures by the formation of V_{Ti}'''' rather than electrons. It serves effectively as a donor dopant, promoting the concentration of electron over all P_{O_2} range. For the Ga-doped case, the Ga_{Ti}' acceptor is predominantly compensated by $Ti_i^{\cdot\cdot\cdot\cdot}$rather than holes, although hole compensation begins to become significant at the highest pO_2s.

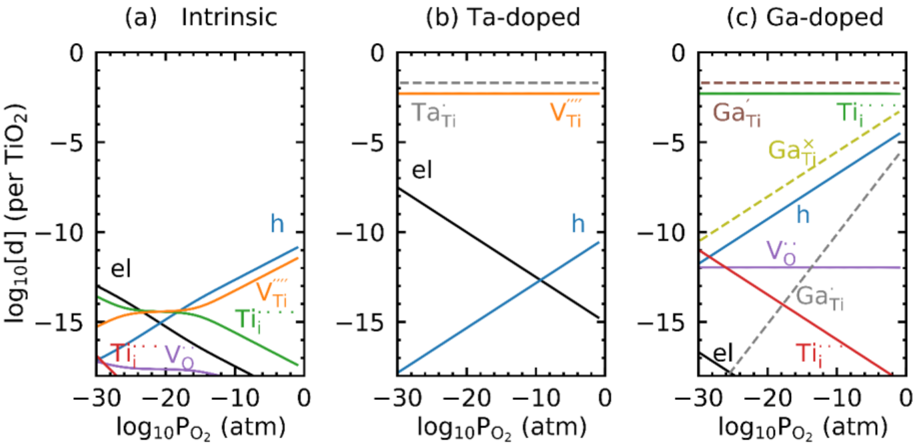

Figure 1: Equilibrium defect concentrations at 600 K for (a) undoped TiO_2, (b) Ta-doped TiO_2, and (c) Ga-doped TiO_2 with varying oxygen partial pressure. For the doped cases, dopant concentrations are fixed to 1%.

With the defect concentration diagrams of the three differently-doped cases, we are in a position to calculate the temperature and pO_2 dependence of the Ti self-diffusivities based on the contributions of both Ti interstitials and vacancies. Figure 2(a) shows the computed Ti self-diffusivity D_{Ti} at pO_2 = 1 atm with respect to $1/T$. Due to the low migration barrier of $Ti_i^{\cdot\cdot\cdot\cdot}$ relative to V_{Ti}'''', it remains as the dominant contributor to D_{Ti} in all three cases. The effective activation energy of D_{Ti} in Ga-doped TiO_2 is considerably lower than that in undoped and Ta-doped cases, given that $[Ti_i^{\cdot\cdot\cdot\cdot}]$ is fixed by Ga doping concentration. In contrast, Ta-doped TiO_2 has the lowest D_{Ti} given tha Ta suppresses the more mobile $Ti_i^{\cdot\cdot\cdot\cdot}$ and therefore here the activation energy includes both the migration energy as well as a high formation energy.

In Figure 2(b) we show the concentrations of the sum of electron and holes calculated at 1200 K for all three cases, as a reflection of the expected total electronic conductivities. For undoped TiO_2, the transition between n-type conductivity and p-type conductivity is predicted to occur at relatively high pO_2 (~ 0.05 atm). This transition pressure is pushed to lower pO_2 with Ga doping, promoting p-type conductivity. For the Ta-doped case, n-type conductivity dominates over the entire pO_2 range. Note that a conductivity plateau is predicted for pO_2s below about 10^{-16} atm, reflecting electron charge compensation for the Ta donor rather than Ti vacancies that occurs at higher pO_2. The predicted plateau starts at a lower pO_2 compared to experimentally reported values, possibly due to the overestimation of reduction enthalpy.

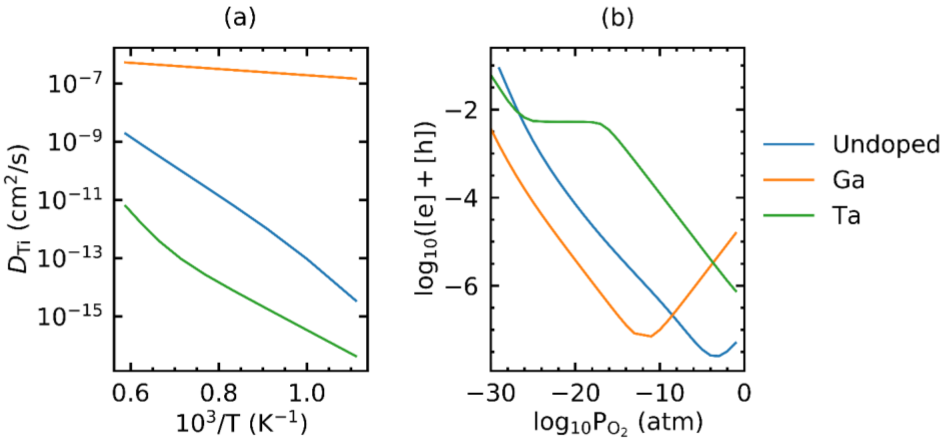

Figure 2: (a) Ti self-diffusivity as a function of temperature at P_{O_2} = 1 atm and (b) electron plus hole concentrations as a function of P_{O_2} at T = 1200 K of the three differently-doped TiO_2 cases.

3.1.2 Modeling of variation of defect formation energy and migration barrier under electric field

With the understanding of how the bulk defect chemistry and cation diffusion kinetics are expected to vary with temperature and pO_2, we further surveyed the effect of electric field on these quantities. Specifically, we computed the formation energies of $Ti_i^{\cdot\cdot\cdot\cdot}$ and $V_{Ti}^{''''}$, and the migration barrier of $V_{Ti}^{''''}$ in the [001] direction with varying electric field. Figure 3 shows how these quantities change with electric field going from 0 to 6 MV/cm. We observe that even with this high electric field strength, the change in formation energies are on the order of 0.01 eV, which has little effect on the equilibrium defect concentrations. The change in migration barrier, as shown in Figure 3(b), appears to be more significant. The barrier decreases from 0.58 eV at zero field to 0.47 eV at E = 6 MV/cm, indicating that we might expect increase in cation diffusivity under strong electric field. However, assuming a typical voltage drop of even 100 mV/GB, and space charge widths of 10 – 100 nm, this represents fields of 0.1 and 0.01 MV/cm respectively, well below fields expected to have a significant effect on defect formation or migration barrier. Much more significant will be changing the dopant type as discussed above.

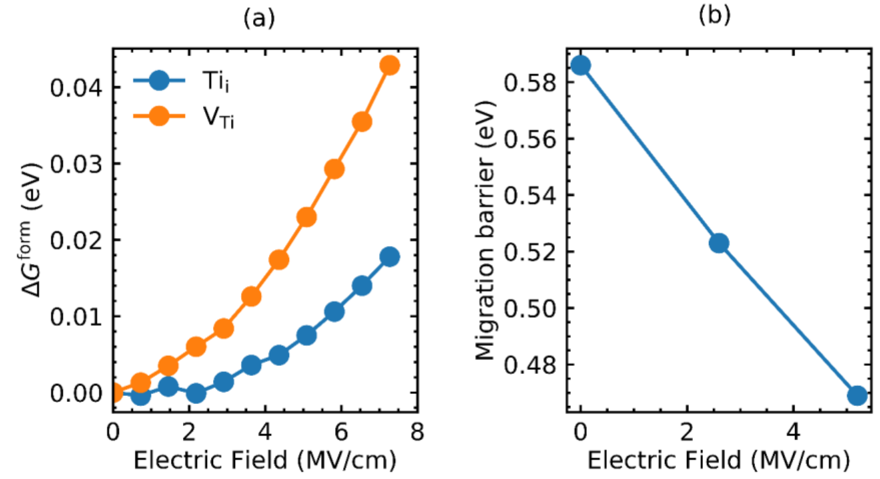

Figure 3: (a) Formation energies of Ti_i and V_{Ti} and (b) migration barrier of Ti_i as a function of electric field strength.

3.1.3 Modeling of mass and charge transport at grain boundaries

Due to the segregation of charged defects to the grain boundary core, defects will redistribute in the vicinity of grain boundaries and form space charge layers. We studied the space charge layer profiles for Ta- and Ga-doped TiO_2 from continuum level modeling in order to understand the different effects they may have in terms of the transport properties of polycrystalline TiO_2.

It has been reported that the dopant type determines the sign of grain boundary space charge in TiO_2 [11]. Specifically, donor dopant segregation leads to positively charged core and negatively charged space charge layer, with a positive space charge potential. The reverse is true for acceptor dopant. In Figure 4 we show the simulated defect redistribution profile for the two doped cases with a space charge potential of 0.3 V for Ta-doped TiO_2 and -0.3 V for Ga-doped TiO_2 at 600 K, 1 atm. In both cases, the dominant type of Ti defect (V_{Ti}'''' for Ta-doped case and $Ti_i^{\cdot\cdot\cdot\cdot}$ for Ga-doped case) accumulates in the space charge layer. The important difference between the two is that, while in both cases the dominant electronic carrier is hole, Ta-doped TiO_2 has depletion of hole in the space charge layer while Ga-doped TiO_2 has accumulation of holes. As a result, grain boundaries are electronically blocking in Ta-doped TiO_2 and conducting in Ga-doped TiO_2.

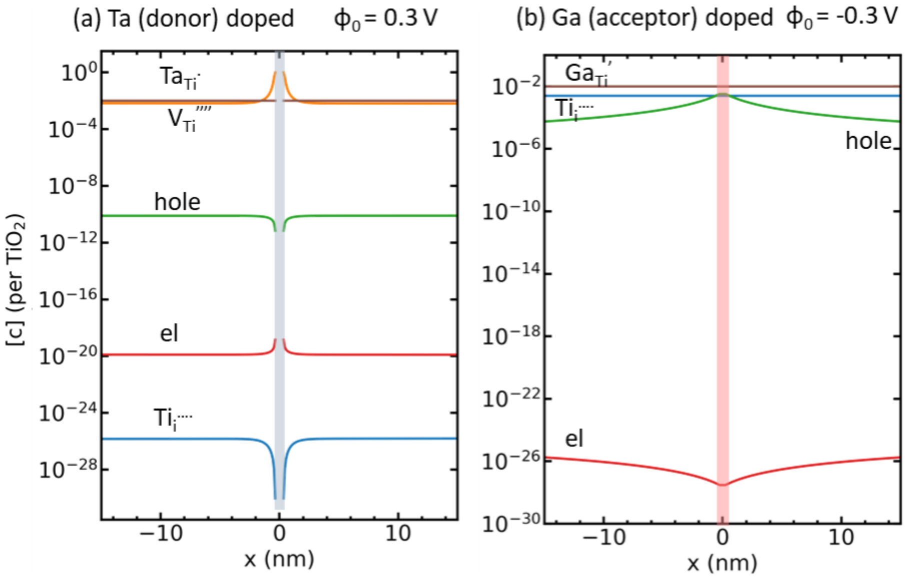

Figure 4: Defect concentration profiles in the space charge layer at T = 600 K, P_{O_2} = 1 atm of (a) Ta-doped TiO_2 assuming a space charge potential of 0.3 V, and (b) Ga-doped TiO_2 assuming a space charge potential of -0.3 V. A grain size of 500 nm is used for the calculation, with the figure showing a range of 30 nm in the vicinity of the grain boundary. The boundary is placed at x = 0.

Another important difference comes up when an external bias is applied across the grain boundary. In Figure 5 we show the electrostatic potential and electric field profile across the grain boundaries with an external bias equivalent to a constant electric field of E = 500 V·cm^{-1} under the same thermodynamic condition as in Figure 5, assuming the grain boundary core charge does not change with the applied bias. We see that because of the high electronic conductivity under the oxidizing condition in Ga-doped one, the applied bias is mostly screened by the electrode/oxide interface and grain boundary, leaving a very small electric field in the grain bulk. On the other hand, Ta-doped TiO_2 is insulating enough that the screening effect due to defect redistribution is negligible. A uniform electric field of 500 V/cm is maintained throughout the bulk of the grains.

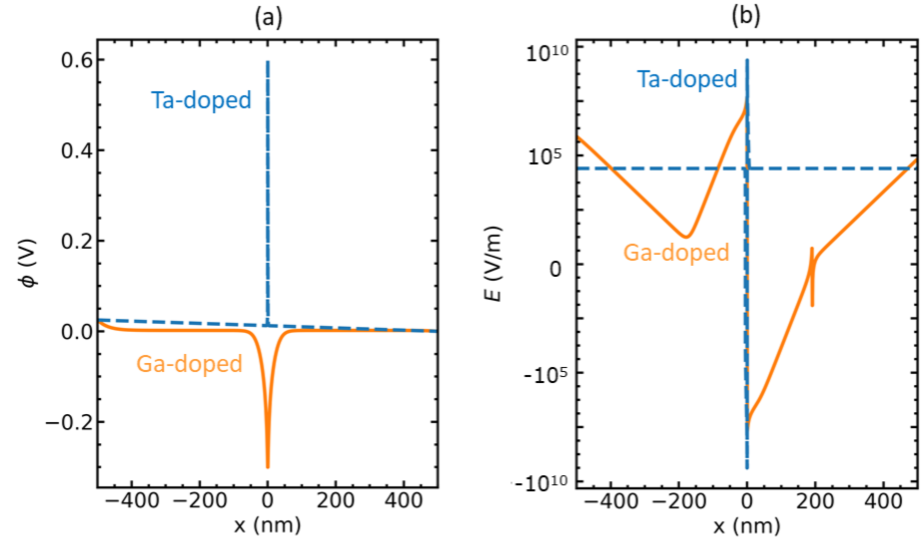

Figure 5: (a) Electrostatic profile, and (b) electric field across the Ta/Ga-doped grain boundaries with an external bias equivalent to E = 500 V/cm at T = 600 K, pO_2 = 1 atm. A grain size of 500 nm is used for the calculation. The boundary is placed at x = 0.

In summary, we have showed two differences between Ta-doped and Ga-doped TiO_2 in terms of space charge effect at grain boundary. Due to the opposite signs of grain boundary space charge potential, grain boundaries in Ta-doped TiO_2 appear to be electronically blocking and grain boundaries in Ga-doped TiO_2 are electronically conducting. Second, because of the difference in total electronic conductivity, external bias is screened by carrier redistribution in Ga-doped TiO_2. This leads to inhomogeneous distribution of electric field in polycrystalline Ga-doped TiO_2 and potentially inhomogeneous Joule heating effect.

3.2 Flash sintering and field assisted sintering experimental results

The experimental effort was focused on trying to confirm the modelling predictions. The experiments can be classified into two main categories: i) flash sintering experiments and ii) field assisted sintering experiments. In the former, a high voltage is applied to the sample as it is heated. As the conductivity increases with increasing temperature, the current density progressively increases, inducing Joule heating. Eventually the sample experiences a thermal and current runaway that leads to a flash (very high temperatures are reached consistent with incandescence) followed by rapid shrinkage of the sample. In the field assisted experiments, the temperature is first increased without the application of an electric field. Once at high temperature (typically 1000 °C), A high current is applied to the sample (0.5-1 A), leading to Joule heating and additional driving force for sintering. As this strategy does not create a thermal runaway, the sample does not flash and the effect of current is much weaker than for the flash experiments. Field assisted sintering is thus easier to control and study systematically than flash sintering. The next section describes the efforts made during this project following these two strategies.

3.2.1 Flash sintering undoped TiO_2

To study the effects of defect concentrations and diffusivities on sintering behavior, we first assessed the feasibility of the flash sintering experiments on undoped TiO_2. The samples were composed of TiO_2 powder pressed into 6 mm diameter pellets (thickness ≈ 3 mm) and pre-sintered at 1050 °C for 3 h. two Pt electrodes were painted on the sides of the pellet to enable the passage of current through the sample. The experiment was done inside a dilatometer, enabling one to follow the shrinkage of the pellet in-situ.

First the electric field was set to 500 $V \cdot cm^{-1}$ at room temperature, and the temperature was increased rapidly to 500 °C. The temperature was then slowly increased by small steps until the flash initiated. When the flash occurs, the power supply reaches its compliance current of 1 A, which is maintained until shrinkage stabilization is reached as measured by the dilatometer. Figure 6 shows the evolution of the shrinkage, current and temperature of the sample during the flash sintering of undoped TiO_2. The first feature is that the thermal runaway effect starts once the current through the sample reaches 10 mA (35 mA·cm^{-2}). Interestingly, the temperature at which the flash happens is dependent on the voltage applied to the sample, but the current at which runaway starts is always around this value of 10 mA. The voltage and temperature are merely two means to reach that critical current density and trigger the runaway effect and flash: a higher voltage will allow passing the critical current at lower temperature, and vice-versa.

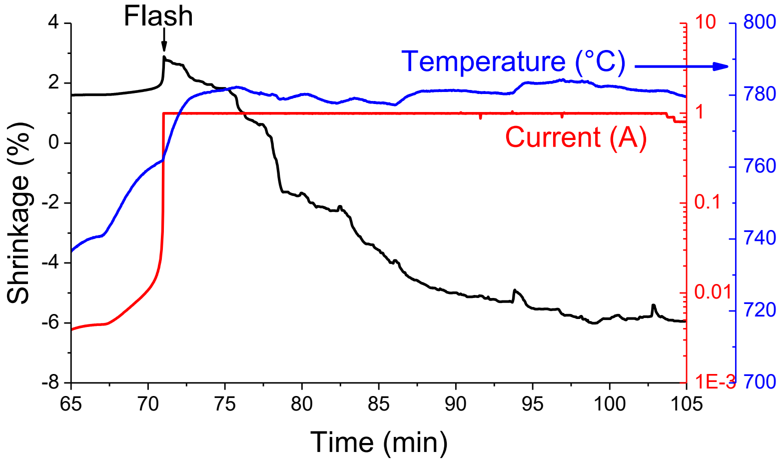

Figure 6: Evolution of the shrinkage, current, and temperature of undoped TiO_2 during flash sintering and application of a voltage of 500 V·cm^{-1}.

The second feature is that the shrinkage of the TiO_2 material is highly non-homogenous, and does not occur in the very short time scales reported in the literature for YSZ [12]. Figure 7 shows a photograph of a TiO_2 pellet following a flash sintering experiment. It illustrates the chaotic character of the sintering, as well as the change in color from white to dark blue. That change in color is due to a reduction of Ti^{4+} to Ti^{3+}, thereby markedly increasing the mobile electron density. The color change is more pronounced at one side of the pellet, which suggest that the reduction of Ti ions is induced by polarization at the negative electrode.

Figure 7: photograph of the undoped TiO_2 pellet after flash sintering.

A more careful microstructural analysis by scanning electron microscopy (Figure 8) reveals that polarization also affects the sintering behavior of the pellet. On Figure 8a, the left side of the pellet is far more thoroughly sintered than the right side. The left side corresponds to the negative electrode where reduction takes place. This well sintered region, corresponding to the reduced side, also expands within a narrow region to the other side of the sample, suggesting a non-homogeneous current pathway through the sample. This further implies that the conductivity must be of a filamentary type, leading in turn to sintering occurring only where the filament progresses. The section of the sample directly adjacent to the well sintered region of the sample is shown magnified in Figure 8b. This zone displays a dendritic structure, pointing to local melting during the experiment. This feature is clear evidence that the local temperature reached by the sample during the flash sintering experiment is extremely high, considering that the melting temperature of TiO_2 is around 1800 °C.

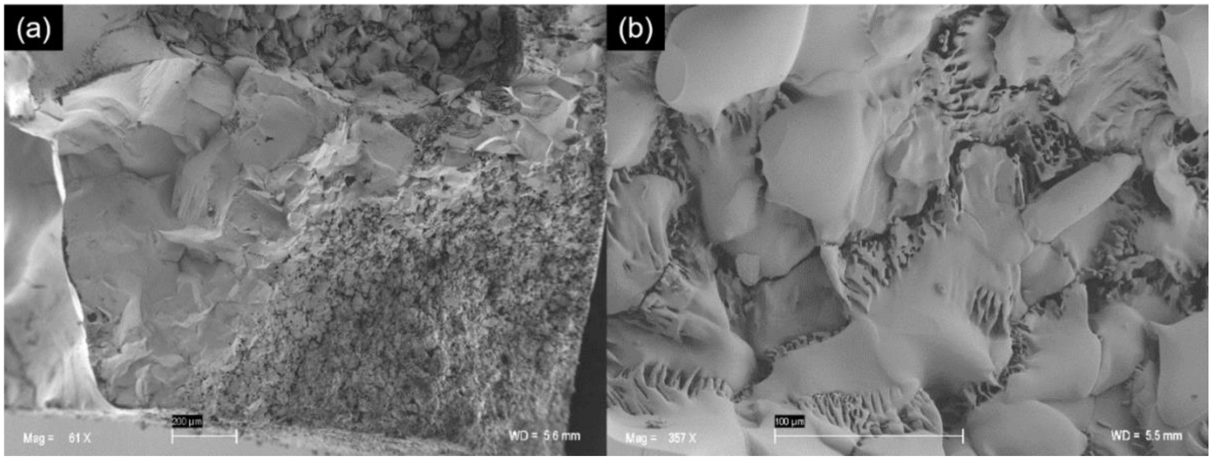

Figure 8: SEM cross section image of a TiO_2 *pellet after flash sintering at* $500 V\cdot cm^{-1}$.

A rough estimation of the local temperature during the flash can be made by examining the resistance of the sample measured during the flash. Figure 9 shows that the conductivity of the sample during the flash (≈ 40 $mS\cdot cm^{-1}$). This corresponds to a temperature of 1400 °C if one considers the extrapolated measured conductivity of TiO_2. As mentioned above, because the flash seems to induce a filament type conduction path, it is reasonable to believe that the temperature increases locally reaching the melting temperature, explaining the dendritic microstructure. Unfortunately, the very high local induced temperatures lead, as well, to the local melting of the Pt electrodes, thereby inducing a loss of the electrical contact.

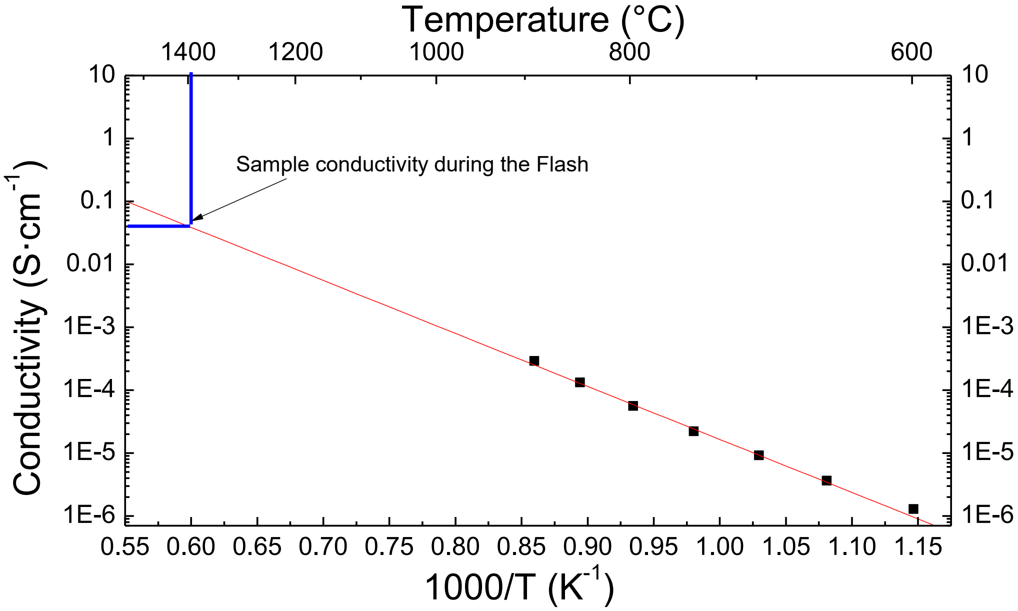

Figure 9: projected temperature during the flash, extrapolated from the conductivity of the sample during the experiment.

Although the flash sintering of TiO_2 is non-homogeneous, the influence of different defect types and concentrations on flash sintering behavior could still be studied. In the following, we report on flash sintering experiments repeated on donor doped TiO_2, to assess the feasibility of the study.

3.2.2 Flash sintering Ta doped TiO_2

Donor doping of TiO_2 is of interest to this study because it allows one to fix the electronic conductivity while varying the types and concentrations of ionic defects responsible for mass transport. In this case, the contribution of Joule heating to flash sintering is fixed by the electronic conductivity with the mobile ionic defect types and concentrations controlling mass transport potentially modifying the sintering behavior. Initially a simple flash sintering experiment was performed to establish whether the behavior of Ta-doped TiO_2 samples would be more homogeneous than un-doped TiO_2, and therefore could be studied more systematically.

Ta-doped TiO_2 (2 at%) powder was prepared by mixing TiO_2 powder with Ta ethoxide in an EtOH solution. After evaporation of the solution, the powder was annealed at 1050 °C for 6 h to allow the Ta to react with and diffuse homogeneously within the TiO_2 lattice. The phase purity of the powder was monitored by X-ray diffraction. The pellet samples for the flash sintering experiments were prepared in the same manner as for undoped TiO_2.

Prior to the flash experiments, the conductivity of the material was measured by impedance spectroscopy. Figure 10 compares the conductivity of undoped TiO_2 and Ta doped TiO_2 (2 %) as a function of temperature. The donor doping of TiO_2 increases the total conductivity by more than 2 orders of magnitude, consistent with values reported by Baumard *et al.* [13] for Nb doped TiO_2. Such a change in conductivity is expected to have a major impact on the behavior of TiO_2 during flash sintering.

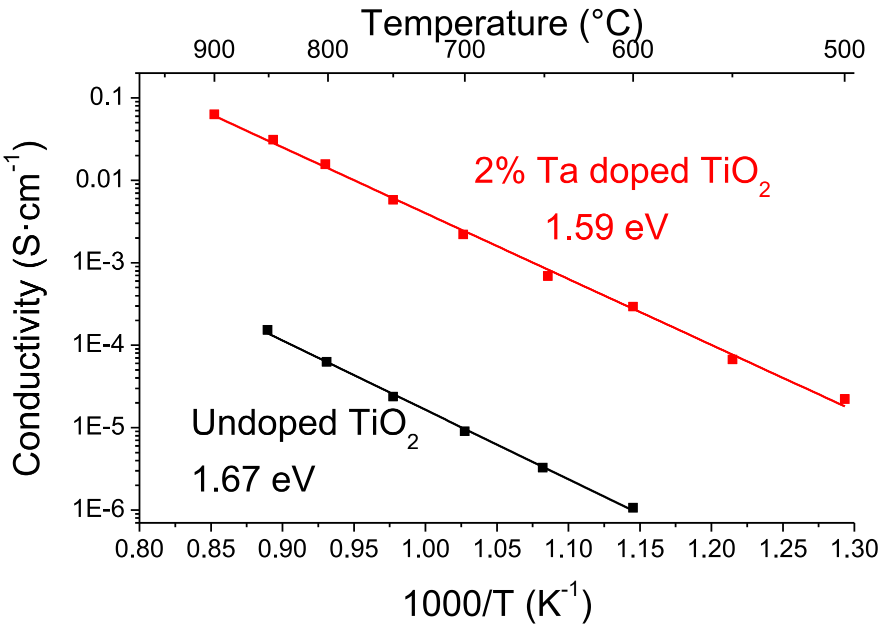

Figure 10: Temperature dependence of the conductivities of undoped TiO_2 *and 2 % Ta:*TiO_2 *measured in air.*

The flash sintering behavior was studied under the same conditions as for undoped TiO_2, *i.e.* 500 V·cm^{-1} was applied at room temperature and the sample was progressively heated until thermal runaway initiated, triggering the flash. Figure 11a shows the evolution of the shrinkage, temperature and current for the Ta doped TiO_2 pellet sample during the flash. The first feature of note is that the onset of thermal runaway just prior to the flash occurs at T_{onset} = 650 °C, that is 110 °C lower than for undoped TiO_2. Although the onset temperature changes, the current at which the runaway initiates is roughly the same as for undoped TiO_2, *i.e.* 10 mA. This again is an indication that the onset of the flash is only dependent on the current passing through the sample, and that the applied electric field and temperature are merely means to achieve this current flow, that depends in turn on the sample resistance, or alternatively its conductivity. However, one finds that even though the flash event occurs, the actual shrinkage of the sample remains very low, even after several hours.

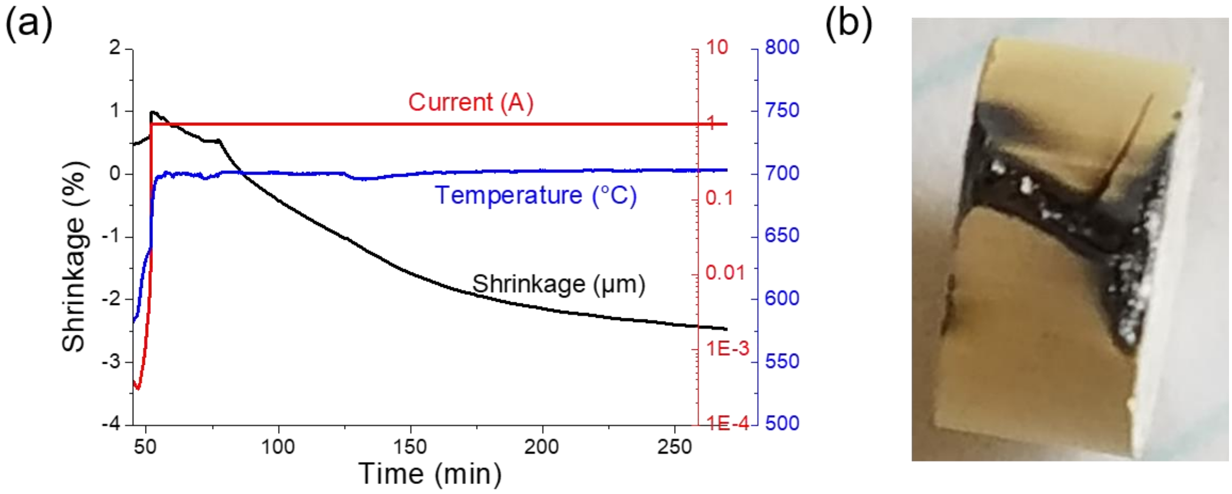

Figure 11: Flash sintering of Ta doped TiO_2 *(2 at%), (a) Shrinkage, temperature and current evolution after the flash at 500 V·cm*$^{-1}$ *(b) photograph of the pellet sample after the flash experiment.*

Examination of the sample following the experiment (Figure 11b) shows a dark strip on one side, indicating that the current path was again spatially limited, similar to a filament type conductivity pathway. Again, the dark color of this filament is a clear indication of a local reduction of the sample. Contrary to undoped TiO_2, the flashed zone in this case remains within this narrow region and does not spread over the whole sample.

Although flash sintering is appealing as a phenomenon because of the possibility of rapid densification of ceramics with moderate energy consumption as compared to classic sintering, we have shown that in the case of TiO_2, densification is not as straightforward as it is in YSZ. Moreover, because of its rather violent character, it induces non-homogeneities in sample shrinkage, thereby rendering the analysis of the influence of defect chemistry on the sintering process difficult. As such, we decided to focus our efforts on designing an alternative experimental protocol. Here we attempt to control the sintering process under electric field but without triggering the flash, in the hope of being able to better control shrinkage and thereby be in a position to study it more systematically as a function of defect types and concentrations.

3.2.3 *Field assisted sintering of Ta-TiO_2 pellets*

To study the influence of mobile ionic defects on the sintering behavior of donor doped TiO_2, we followed a strategy of so-called field assisted sintering, which does not trigger the flash, in order to achieve better control of the sintering process. The objective was to compare the sintering behavior of donor doped TiO_2 under different pO_2 conditions to either change the electron concentration [*n*], and therefore the influence of Joule heating on the sintering, or the concentration of cationic defects (interstitials of vacancies) at a fixed [*n*] (and fixed joule heating). Figure 12a shows the Brouwer defect diagram of donor doped TiO_2, which serves as a guide for selecting the conditions of pO_2 and temperature at which the field assisted sintering experiments would be done. In the oxidizing region at high pO_2, the cation defects are fixed by The Ta dopant (Ti vacancies) while the electron density n changes with pO_2. As a consequence, the effect of Joule heating can be studied in this region, without having an influence of a change in ionic defect concentration. In the intermediate pO_2 region, on the other hand, *n* is fixed by the dopant concentration, as will be the resistance of the specimen and in turn the Joule heating, but the type and concentration of ionic defects will change. This region allows one to study the effects of defect type and concentration on the sintering behavior. As demonstrated by the modeling study, Ti interstitials should diffuse and drift faster than vacancies, so sintering should be faster when operating on the left hand side of the plateau than on the right hand side, where Ti vacancies dominate. Also, moving from the sides to the middle of the plateau close to stoichiometry where the total concentration of Ti defects are at a minimum could also be expected to substantially modify the sintering behavior.

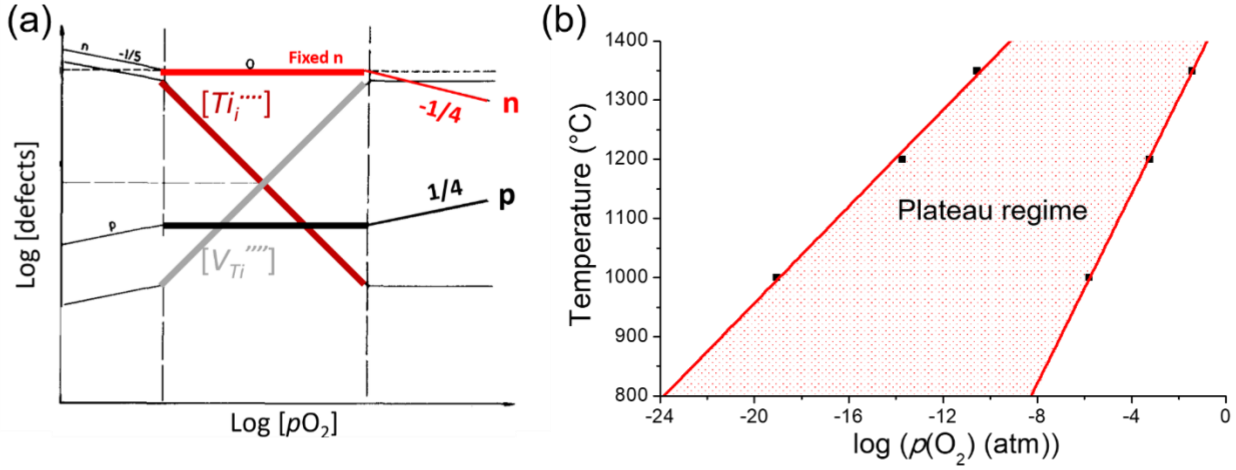

Figure 12: (a) Brouwer diagram of donor doped TiO_2, reproduced from [13] and (b) calculated plateau regime.

From the work Baumard *et al.* [13], it is possible to calculate what widths of the pO_2 plateaus as a function of temperature and dopant level. Figure 12b shows the calculated plateau region for different temperatures assuming a 2% Ta doping level. For field assisted sintering experiments being done at 1000 °C, the plateau regime is calculated to apply between $10^{-19} < pO_2 < 10^{-6}$ atm.

The Ta doped TiO_2 pellets where heated inside the dilatometer up to 1000 °C at various pO_2 in the oxidized and intermediate regime, first without application of electric current. The samples were stabilized at this temperature for one night to equilibrate with the pO_2 and to reach a steady expansion (some small degree of sintering can occur prior to the application of the current). Then a current of 500 mA was applied to the sample with the shrinkage recorded for 150 min. Figure 13 compares the resulting shrinkages of four samples at 4 different pO_2. First, comparing the shrinkage in air (Figure 13a) and at 2×10^{-5} atm (Figure 13b) illustrates the effect of the Joule heating at a constant ionic defect concentration (oxidizing region). The shrinkage in air is roughly 20 µm while only 6 µm at $pO_2 = 2\times10^{-5}$ atm, because at constant current, the voltage drop in air is higher and so is the power dissipated in the sample. Because the temperature is measured with a thermocouple close to the sample (but not touching), the change in measured temperature is not precise, and is likely much higher inside the sample. Comparing the shrinkage at $pO_2 = 2\times10^{-5}$ atm (Figure 13b) and at $pO_2 = 1\times10^{-14}$ atm (Figure 13c) shows the influence of the defect type on shrinkage. Because $pO_2 = 2\times10^{-5}$ atm is close to the beginning of the plateau regime, it should represent conditions for which one obtains the highest concentrations of Ti vacancies, while being very close to the constant concentration of [n]. At $pO_2 = 1\times10^{-14}$ atm on the other hand, one instead expects largely Ti interstitials. In the latter, the shrinkage of 9 µm is nearly twice as high as in the former, which agrees with the modeling results showing that the Ti interstitials diffuse faster than Ti vacancies. By repeating the experiment at lower pO_2, *i.e.* $pO_2 = 3\times10^{-16}$ atm (Figure 13d) the measured shrinkage is slightly higher than $pO_2 = 1\times10^{-14}$ atm, also consistent with the defect model, because the lower pO_2 increases $[Ti_i]$, which should lead to increased mass transport.

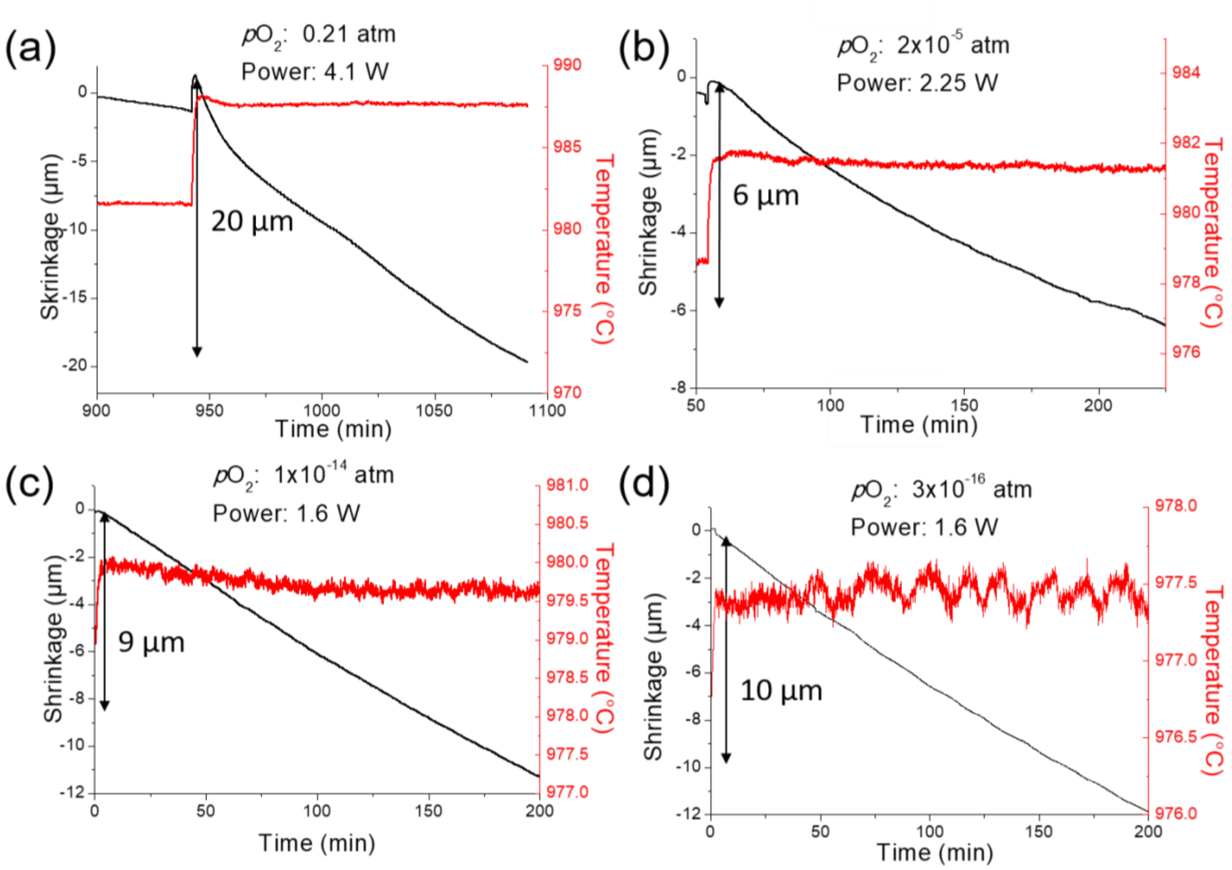

Figure 13: Shrinkage of Ta doped TiO2 pellet at 1000 °C with an applied current of 500mA, as a function of time, at different pO_2 values: (a) $pO_2 = 0.21$ atm, (b) $pO_2 = 2\times10_{-5}$ atm, (c) $pO_2 = 10_{-14}$ atm, and (d) $pO_2 = 3\times10_{-16}$ atm.

These field assisted experiments effectively enable examination of the influence of defect type and concentration on shrinkage, with the results agreeing well with predictions made based on the defect model and the diffusivities of each defect calculated in the modeling part. However, measured shrinkages are rather small, and thus the reliability of such results can be questioned. The problem of the experimental protocol is that the geometry of the sample yields very low resistances at the plateau regime, thereby limiting the power that can be applied to the sample, considering limitation of the power supply. Further, if the sample resistance becomes on the order of magnitude of the lead and contact resistance, a considerable fraction of the power will dissipate elsewhere than inside the sample itself.

To overcome the problem associated with low resistance samples, a second strategy was considered. Here the geometry of the samples is modified to increase their resistances thereby allowing for the ability to apply higher electrical power densities.

3.2.4 Field assisted Ta doped TiO_2 screen printed layers

By preparing porous thin layers of Ta doped TiO_2 by screen-printing (≈ 50 µm), it is possible to increase the resistance of the samples given the much reduced cross sectional area. This serves to increase the power density applied to the sample, thereby improving the sensitivity of the measurements. The layers were printed on sapphire substrates (MTI, c-plane). Pt paste was applied on both sides to serve as current collectors (Figure 14). The samples were heated to 980 $_{o}$C for one night to equilibrate the initial shrinkage and then the electrical power was applied to induce sintering. The shrinkage of the layer was measured by a dilatometer in the same setup used for the pellet-based experiments.

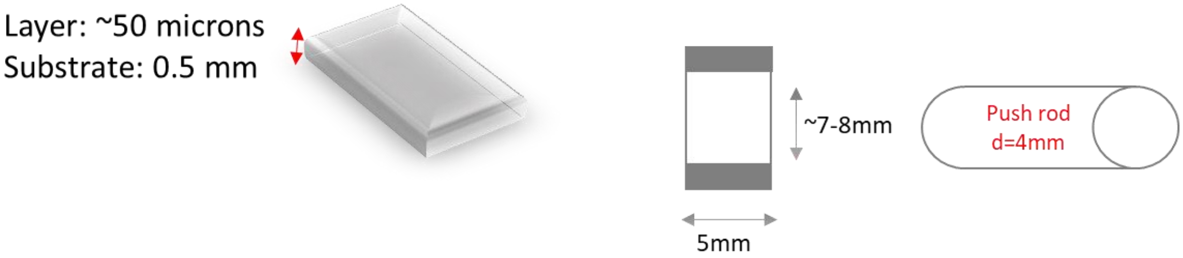

Figure 14: Sample configuration

A power density of around 800 W·cm^{-3} was applied through voltage and current control, and was calculated a-priori with respect to the resistance of the layer. In the first stage of the experiment, the application of the current induced joule heating results also in the expansion of the sapphire substrate, leading to an overall thermal expansion of the layer/substrate composite. This rapid expansion can be largely attributed to the expansion of the substrate, with a negligible contribution from the much thinner layer. This initial expansion can be used to estimate the temperature increase induced by the application of the current, based on the expansion coefficient of the sapphire substrate according to the expression:

$$\Delta L/L = \Delta T \cdot \alpha$$

With $\Delta L/L$ the linear shrinkage, α the expansion coefficient, and ΔT the corresponding change in temperature. The temperature increase for an applied power density of 800 W·cm^{-3} was estimated on this basis to be ~ 200 °C. This then corresponds to a sample temperature ≈1200 °C during the experiment.

Following this initial stage, the power is kept constant for 20 hours, while the sintering of the screen printed layer is monitored. This experiment was repeated at different pO$_2$, following the same strategy as for the pellet samples. Figure 15 shows the shrinkage of the layers as a function of oxygen partial pressure after applying ~800W/cm^3 for 20 hours at 980^{o}C. As observed with the pellets, while under a constant power density, the pO$_2$ has a significant effect on the shrinkage of the layers, because of the change in the dominant defect type and concentration. Close to the stoichiometric point, shrinkage is lowest. When increasing pO$_2$, the concentration of Ti vacancies increases and the shrinkage is enhanced. When pO$_2$ is reduced to pO$_2$=10^{-15} atm, the dominant defect switches to Ti interstitials and the shrinkage is greatly enhanced, which is consistent with the modeling results showing that interstitials have a much smaller migration barrier than that of vacancies.

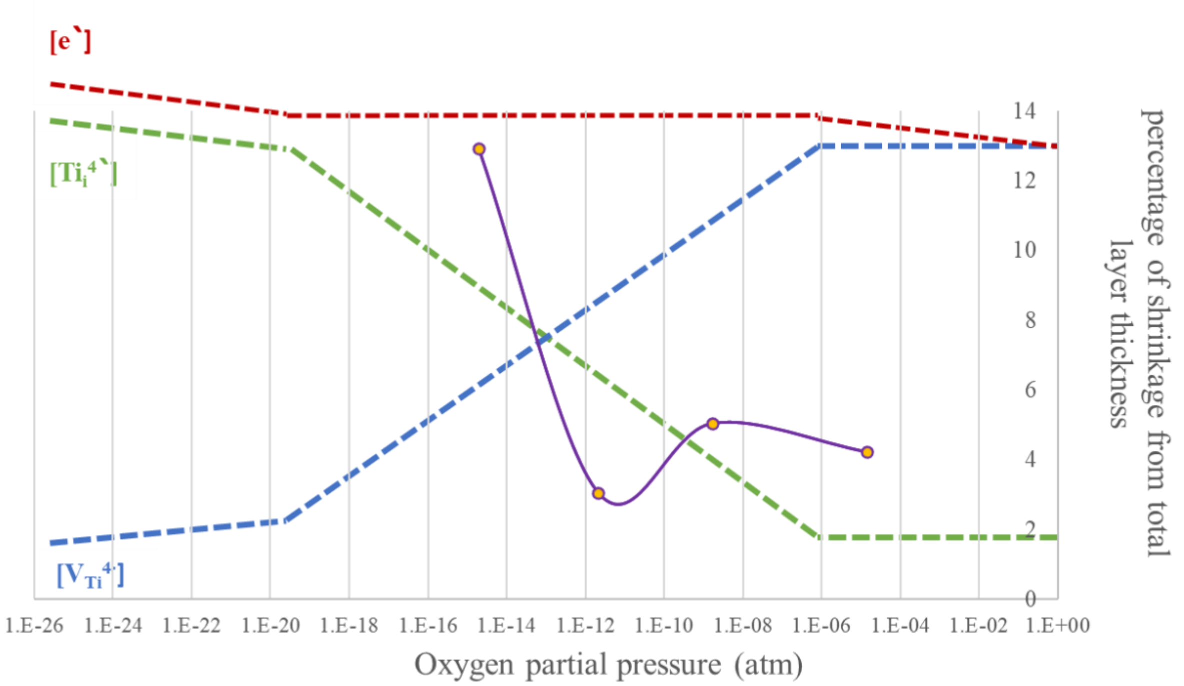

Figure 15: Percentage shrinkage of Ta-doped TiO_2 layers vs. oxygen partial pressure, after applying ~800W/cm_3 for 20 hours at 980_oC. The plot is overlaid on the Brouwer's defect diagram (qualitative), presenting the variation in defect concentration of the 3 main charge carriers participating in charge conductivity and/or diffusion.

This strategy led to similar conclusions as those based on measurements performed on pellet samples, but the relative shrinkage measured is far higher, which makes the results measured on screen printed more reliable.

4 Conclusions

This project allowed us to gain greater insight into the underlying mechanisms that occur during field assisted sintering. Using TiO_2 as a model system allows one to engineer the main defect types and concentrations through doping and pO_2 management. The modeling of the migration barrier for diffusion of Ti defects shows that interstitials diffuse considerably faster than Ti vacancies, and that an external electric field, such as those used in flash sintering experiments (500 V·cm$_{-1}$), has little influence on the migration barrier. Consequently, the leading mechanism explaining enhanced sintering under electrical bias can be attributed largely to Joule heating. The effect of the space charge at the grain boundaries was also modeled in the case of donor or acceptor doped TiO_2, and showed that grain boundaries are electronically blocking in Ta-doped TiO_2 and conducting in Ga-doped TiO_2, which can also play an important role related to heat dispersion induced by Joule heating. We also show that an applied electric field will be non-homogeneous in Ga-doped TiO_2 because of carrier redistribution. The flash sintering experiments were found to be difficult to reproduce due to the generation of non-homogeneous current pathways via conductive filaments. The temperatures reached during flash are potentially high enough to trigger local melting of TiO_2. Measurements of field assisted sintering with moderate applied electric fields makes the study of the influence of defect concentration on sintering feasible. With the two strategies considered, *i.e.* pellets and thick film measurements, we show that sintering is enhanced when Ti interstitials are the dominant defects, in accordance with the results of defect migration barrier modeling

Summarizing the key findings of this study, field assisted sintering of semiconducting oxides is largely driven by joule heating. Optimum results can be expected, i.e. lowest furnace temperature and shortest sintering times, when dopants and oxygen partial pressure are selected that support the fastest migrating ionic species limiting densification. Furthermore, selection of geometry is critical in insuring that sufficient Joule heating is achieved and that current flow is uniform across the densifying ceramic element.

Acknowledgments: Funding by the Army Research Office (ARO) via award (6936242) under the supervision of Dr. Michael P. Bakas is much appreciated. Dr. Clement Nicollet was responsible for specimen preparation, electrical and dilatometric studies, microstructural analysis and data interpretation with assistance from Ms. Tamar Kadosh. Modeling was performed by Ms. Jing Yang and Mr. Minh Dinh. Professors Harry Tuller and Bilge Yildiz supervised the research activities.

5 References

[1] G. Kresse and J. Hafner, Physical Review B 47, 558 (1993).
[2] G. Kresse and J. Hafner, Physical Review B 49, 14251 (1994).
[3] G. Kresse and J. Furthmüller, Computational Materials Science 6, 15 (1996).
[4] G. Kresse and J. Furthmüller, Physical Review B 54, 11169 (1996).
[5] J. P. Perdew, K. Burke, and M. Ernzerhof, Physical Review Letters 77, 3865 (1996).
[6] J. P. Perdew, K. Burke, and M. Ernzerhof, Physical Review Letters 78, 1396 (1997).
[7] S. L. Dudarev, G. A. Botton, S. Y. Savrasov, C. J. Humphreys, and A. P. Sutton, Physical Review B 57, 1505 (1998).
[8] M. Youssef and B. Yildiz, Physical Review B 86 (2012).
[9] R. W. Nunes and X. Gonze, Physical Review B 63, 155107 (2001).
[10] S. B. Zhang and J. E. Northrup, Physical Review Letters 67, 2339 (1991).
[11] J. A. S. Ikeda, Y.-M. Chiang, A. J. Garratt-Reed, and J. B. V. Sande, Journal of the American Ceramic Society 76, 2447 (1993).
[12] M. Cologna, B. Rashkova, and R. Raj, J. Am. Ceram. Soc., 93 [11] 3556–3559 (2010)
[13] J.F. Baumard and F. Tani, The Journal of Chemical Physics 67, 857 (1977).